JOURNAL OF GEOPHYSICAL RESEARCH, VOL. 104, NO. D8, PAGES 9663–9670, APRIL 27, 1999

Propagation delays induced in GPS signals by dry air, water vapor, hydrometeors, and other particulates

Fredrick S. Solheim and Jothiram Vivekanandan
Research Applications Program, National Center for Atmospheric Research, University of Colorado, Boulder

Randolph H. Ware
GPS Science and Technology Program, University Center for Atmospheric Research, Boulder, Colorado

Christian Rocken
COSMIC Program, University Center for Atmospheric Research, Boulder, Colorado

Abstract. Dry air, water vapor, hydrometeors, and other particulates (sand, dust, aerosols, and volcanic ash) in the atmosphere introduce microwave propagation delays. These delays must be properly characterized to achieve the highest accuracy in surveying and atmospheric sensing using Global Positioning System (GPS) signals. In this paper we review the theory of microwave propagation delays induced by the above atmospheric constituents and estimate their maximum delays. Because the structure of atmospheric refractivity can be highly complex and difficult to model, and because measurement tools are unavailable for characterizing most of the refractive components, we use simplified examples to illustrate its effects. Our results show that propagation delays due to water vapor, cloud liquid, rain, and sandstorms can be significant in high-accuracy GPS applications. For instance, propagation through 1 km of heavy rain can induce 15-mm delays in L_1, and because delays due to scattering are dispersive and alias as ionospheric delays in L_3 processing, L_3 range errors are magnified to 20 mm. Depending upon the distribution of precipitation relative to the configuration of GPS satellites, such unmodeled delays can induce horizontal and vertical errors of several centimeters.

1. Introduction

Microwave signals transmitted by Global Positioning System (GPS) satellites are increasingly used for high-accuracy scientific applications including studies of weather, climate, crustal deformation, plate tectonics, sea level, ice dynamics, and isostasy. The 24 GPS satellites broadcast 1.575 (L_1) and 1.228 (L_2) GHz carriers based on atomic clocks. Receivers for high-accuracy tracking of these two carriers are commercially available at relatively low cost. *Spilker* [1978] describes GPS, and *Herring* [1996] describes scientific applications of GPS. GPS surveying over distances of 50 km or more has been routinely achieved with centimeter precision [*Segall and Davis*, 1997], and in some cases, where atmospheric delays are properly corrected, it has been demonstrated with millimeter precision [*Ware et al.*, 1993; *Alber et al.*, 1997]. In addition, the use of ground- and space-based GPS receivers for atmospheric sensing is rapidly increasing. Ground-based GPS receivers can sense column water vapor [*Bevis et al.*, 1992; *Solheim*, 1993; *Rocken et al.*, 1993, 1995, 1997a; *Businger et al.*, 1996] and integrated water vapor along GPS ray paths [*Alber*, 1996; *Ware et al.*, 1997]. Space-based GPS receivers using the radio occultation method [*Melbourne et al.*, 1994] can sense atmospheric temperature, pressure, and water vapor profiles [*Ware*, 1992; *Yuan et al.*, 1993; *Ware et al.*, 1996; *Kursinski et al.*, 1996; *Rocken et al.*, 1997b; *Kuo et al.*, 1998]. In order to achieve the best-accuracy GPS measurements, the effects of various atmospheric constituents are important. In this paper we review the physics and estimate the magnitude of GPS propagation delays generated by dry air, water vapor, hydrometeors, hygroscopic aerosols, sand, and volcanic ash.

Paper number 1999JD900095.
0148-0227/99/1999JD900095$09.00

2. Background

Atmosphere-induced propagation path delays and unmodeled multipath are major contributors to GPS measurement error [*Meertens et al.*, 1997]. Water vapor is typically the largest source of variable atmospheric delay. Changes in the distribution of water vapor are associated with clouds, convection, and storms. In addition, variations resulting from orographic, frontal, coastal, and seasonal gradients may be present. A "stochastic" method minimizes survey error by fitting atmospheric delays during GPS antenna coordinate determination. The method generally models an isotropic atmosphere using a mapping function [*Niell*, 1996] and does not consider horizontal atmospheric gradients. More complex models would require a more sophisticated approach to resolve additional atmospheric parameters. Special cases dealing with complex modeling or independent measurement of atmospheric anisotropies are discussed by *Davis et al.* [1993], *Ware et al.* [1993, 1997], *Alber et al.* [1997], and *Bar-Sever et al.* [1998]. Antenna design and placement can significantly reduce multipath errors [*Solheim et al.*, 1997], and atmospheric delay errors can be reduced through modeling and correction with pointed radiometers [*Ware et al.*, 1986; *Solheim*, 1993; *Ware et al.*, 1993; *Alber et al.*, 1997].

Zenith path delay can be expressed as

Table 1. Typical High Values of Zenith Path Delay at Sea Level

Source	Magnitude, cm	Scale Height, km
"Dry" air	250	~8
Water vapor	45	~2 (typical)
Hydrometeors	1.5	variable
Volcanic ash	0.04	variable

$$\text{ZD (mm)} = \int_0^\infty N dz \tag{1}$$

where $N = 10^6 (n - 1)$ is refractivity, n is the index of refraction, and z is the vertical signal path in kilometers. Typical high values of zenith GPS propagation delays are listed in Table 1, based on calculations described later.

Atmospheric delay as a function of elevation angle can be calculated using mapping functions. A simple mapping function for a plane parallel medium is the cosecant of the elevation angle. At low elevation angles, atmospheric curvature and ray bending require more complex mapping functions such as those described by *Niell* [1996]. However, at low angles, mapping functions may not adequately model highly variable delays induced by water vapor and hydrometeors.

In the following sections we give a mathematical formulation for atmospheric refractivity including the individual contributions from dry air, water vapor, hydrometeors, and other particulates. We also characterize their size, concentration, and delays.

3. Refractive Radio Phase Path Delays

Refractive delays are induced by the ionosphere and the neutral atmosphere. Refraction in the ionosphere is dispersive and therefore can be corrected using dual-frequency GPS measurements [*Spilker*, 1978; *Brunner and Gu*, 1991; *Ware et al.*, 1996]. In the neutral atmosphere, delays are induced by refractivity of gases, hydrometeors, and other particulates, depending on their permittivity and concentration, and forward scattering from hydrometeors and other particulates. In this section we focus on refractive delays induced in the neutral atmosphere. Scattering delays are discussed in section 3.4.

In dry air, refractivity is proportional to air mass in the propagation path and is therefore predictable from atmospheric pressure. In the presence of water vapor and hydrometeors, refractivity can be modeled with the aid of additional measurements. Refractivity can be separated into nondispersive and dispersive components. The dispersive component depends on molecular resonances in the vicinity of the propagation carrier frequency. Since GPS carrier frequencies are far removed from molecular resonances, their influence can be ignored. In general, the total refractivity can be expressed as

$$N(f) = N_0 + N'(f) + iN''(f) \tag{2}$$

where f is frequency, N_0 and $N'(f)$ are the nondispersive and dispersive parts of refractivity related to the real part of the permittivity, and $N''(f)$ is attenuation and is related to the imaginary part of the permittivity.

Refractivity in cloud droplets, rain, snow, and haze is due to displacement of charge in the dielectric medium and to scattering. Polar atmospheric gases and hydrometeors contribute to nondispersive atmospheric refractivity. In atmospheric gases the refractivity is due to displacement of the electron cloud of the gaseous constituents and, additionally, to alignment of electrically and magnetically polar molecules with the propagated electric and magnetic fields. Significant electrically polar molecules include water vapor, some oxides of nitrogen, and many chlorine and organic compounds. With the exception of water vapor the partial pressure of significant polar molecules is essentially constant in the atmosphere. The only significant atmospheric molecule with a magnetic moment is oxygen.

In the following sections, delays are separated into those induced by the "dry" (without water or water vapor) atmosphere, water vapor, hydrometeors, aerosols, volcanic ash and sandstorms, and scattering.

3.1. Phase Delay Induced by the "Hydrostatic" Atmosphere

The largest atmospheric delay results from "hydrostatic" constituents (gases excluding water vapor). The hydrostatic delay is directly proportional to atmospheric pressure and can be accurately modeled. The hydrostatic refractivity can be expressed as [*Thayer*, 1974]

$$N_{\text{dry}} = k_1 \frac{P_d}{T} \tag{3}$$

where $k_1 = 77.6$ K mbar^{-1}, P_d is the hydrostatic air pressure in millibars, and T is temperature in kelvins. Using the hydrostatic equation and integrating vertically through the atmosphere, we obtain for the total hydrostatic zenith delay

$$\text{ZD}_{\text{hydrostatic}}(\text{cm}) = k_1 \int_0^\infty \frac{P_d}{T}\, dh = 77.6 R_d \int_0^\infty \rho(h)\, dh$$

$$= 77.6 \frac{R_d P_s}{g} \tag{4}$$

where g is the location-dependent gravitational constant, P_s is surface pressure in millibars, ρ is density in g cm^{-3}, and $R_d = 2.87 \times 10^6$ cm^2 s^{-2} K^{-1} is the gas constant for dry air. A barometric measurement therefore can be used to estimate the zenith hydrostatic delay. If the barometric pressure is known to 1 mbar, zenith hydrostatic delay can be estimated with an accuracy of 2.3 mm.

3.2. Phase Delay Induced by Water Vapor

The second largest contributor to tropospheric delay is water vapor. It is also the most highly variable component of delay. The wet refractivity of water vapor can be expressed as

$$N_{\text{vap}} = k_2 \frac{P_v}{T} + k_3 \frac{P_v}{T^2} \tag{5}$$

where $k_2 = 64.8$ K mbar^{-1}, $k_3 = 3.776 \times 10^5$ K^2 mbar^{-1}, P_v is the partial pressure of water vapor (e) in millibars, and T is in Kelvins [*Thayer*, 1974]. The second term in this expression results from the dipole moment of water vapor and is ~20 times larger than the first term. The (temperature dependent) phase delay is approximately 6.5 times the path-integrated water vapor [*Hogg et al.*, 1981]. Normally, P_v values are less than 12 mbar, although values as much as 40 mbar can occur at high temperatures. Integrated water vapor is directly measurable with radiometers, Lidars, Fourier transform infrared spectrometers, and radiosondes.

3.3. Phase Delay Induced by Nongaseous Atmospheric Constituents

Line shape and intensity measurements and models of the permittive atmospheric components have evolved and have been improved [*Debye*, 1929; *Van Vleck*, 1932; *Becker and Autler*, 1946; *Gross*, 1955; *Waters*, 1976; *Liebe*, 1989; *Keihm et al.*, 1995], thereby facilitating their accurate measurement and application to high-accuracy GPS measurements. Stochastic estimation and direct measurement of water vapor have improved GPS surveying accuracy to the millimeter level under some circumstances [*Dixon*, 1991; *Alber et al.*, 1997]. Because of the success in diminishing uncertainties due to water vapor and other sources of error, delays due to liquid and ice phase water are becoming relatively significant. Phase delays due to hydrometeors and other particulates can be significant in high-accuracy GPS measurements. Hydrometeors are defined as particles (such as fog, rain, hail, snow, and graupel) formed by the condensation of atmospheric water vapor. Other particulates that we consider in this paper are aerosols, dust, sand, and volcanic ash. While the delay from water vapor is due to the polar nature of the water molecule, phase delays induced by cloud droplet and aerosol particles smaller than 1 mm in size can be approximated using calculations based on permittivity. For larger particles, calculations of forward scattering should be included. For nongaseous and nonscattering (<1 mm for GPS) particles, we can use the Clausius-Mossotti equation for refractivity [*Debye*, 1929; *Van de Hulst*, 1957; *Liebe et al.*, 1989; *Born and Wolf*, 1986, chapter 2]:

$$(n - 1) \times 10^6 = N = 1.5 \times 10^6 \frac{M}{\rho}\left[\frac{\varepsilon - 1}{\varepsilon + 2}\right] \qquad (6)$$

where M is the mass content of the particles per unit of air volume, ρ is the density of the particles (both in the same units of mass per unit volume), ε is the permittivity of the particles, and M/ρ is the mass fraction of the suspended particles.

3.3.1. Phase delay approximations based on permittivity for cloud, fog, and haze. By the Clausius-Mossotti equation, dielectric refractivity is proportional to the total liquid along the propagation path and is independent of the shape of the cloud droplet [*Born and Wolf*, 1986; *Jackson*, 1975]. The permittivity of water is a weak function of temperature. Liquid water exists over a range of atmospheric temperatures (−15° to 20°C), and the permittivity for liquid water varies from about 92 to 74. Since permittivity dominates both the numerator and the denominator in the following expression, however, we can approximate to within 1%:

$$N_{\text{cloud}} = \frac{3}{2}\frac{M_l}{\rho_l}\left[\frac{\varepsilon_0 - 1}{\varepsilon_0 + 2}\right] = 1.45 M_l \qquad (7)$$

where M_l is the mass content of cloud water per volume of air along the propagation path in g m^{-3}, ρ_l is the density of water (~1 g cm^{-3}), and ε_0 is the permittivity of water.

The subscript l is used to describe all forms of suspended liquid water including cloud droplets, fog, and haze. Recall that the refractivity N is the deviation from the in vacuo value of propagation velocity in parts per million. A convenient scale of N for meteorological features whose dimensions are of the order of kilometers is mm km^{-1}. A cloud droplet concentration of 1 g m^{-3} for a distance of 1 km has an integrated liquid value of 1 mm and would therefore induce a radio path delay of 1.45 mm.

A direct measurement of the path integral of liquid water is available from microwave radiometers. Such a measurement is routinely made by multichannel water vapor radiometers to make them usable in the presence of liquid water [*Hogg et al.*, 1983; *Solheim et al.*, 1998].

3.3.2. Phase delay approximations based on permittivity for aerosols. The assimilation of water by hygroscopic aerosols is a function of relative humidity. Provided that the condensation nucleus of the aerosol does not affect the permittivity of the aerosol droplet, the radio phase delay of aerosols is, like other liquid phase droplets, proportional to the bulk concentration of water. Such aerosols tend to lie in the boundary layer and therefore generally involve only several hundred meters of propagation path length. Additionally, normal concentrations are ≤0.1 g m^{-3} [*Liebe*, 1989]. Aerosols therefore induce path delays of less than 0.1 mm, even if any contained solute drastically increases the permittivity, and can therefore be ignored except for very long paths.

3.3.3. Phase delay approximations for sandstorms. Sandstorms are of concern to satellite telemetry and were therefore included in this survey. They are frequent in some locations and nonexistent over most of the world. They can be a significant contributor to carrier depolarization and phase delay. Depolarization can exacerbate antenna multipath because the circular polarization of the carrier is degraded, making the antenna rejection of reflected GPS signals less effective. Sand and dust contained in sandstorms have permittivities of about 4, depending upon moisture content, about 5% of the permittivity of water. An extreme sandstorm lofts densities up to about 40–60 g m^{-3}, creating visibilities of 4–5 m [*Goldhirsch*, 1982]. This yields a refractivity of

$$N_{\text{sand}} \approx 18 \qquad (8)$$

Such heavy sand and dust loading would induce delays of 18 mm km^{-1} of propagation path within the sandstorm. Scattering delays are insignificant because of the small particle size. Sandstorms rarely loft material more than 3 km.

3.3.4. Phase delay based on permittivity of volcanic ash cloud. Volcanic ash cloud is composed primarily of silica. The size distribution of ash particulates is highly variable and coexists with water and ice clouds soon after the eruption. Roughly 12 hours after the eruption, the ash particle size can be represented using a lognormal distribution with effective radius between 0.1 and 20 μ [*Wen and Rose*, 1994]. The density of a typical ash particle (ρ_A) is 2.6 g cm^{-3}, and the amount of ash (P_A) might vary between 0.04 and 0.0002 g m^{-3}. The real part of the permittivity of ash particles is $\varepsilon_A = 6$, for frequencies less than 20 GHz, and the path-integrated ash is of the order of 0.04 cm [*Adams et al.*, 1996]. From the Clausius-Mossotti equation the delay due to an ash cloud is smaller than 0.01 cm for the above case. There may be significant water vapor release associated with volcanism that can induce delays.

3.4. Radio Propagation Delay Induced by Scattering From Rain, Hail, and Snow

Forward scattering from sparsely distributed discrete particulates causes phase delay. As is shown by *Tranquilla and Al-Rizzo* [1994], scattering effects upon GPS baseline measurements are minimal if the scattering environments are the same at the ends of the baselines, but precipitation is rarely so uniform, and precipitation in the vicinity of the antennas can cause significant errors. The real part of the forward scattering amplitude is proportional to the phase delay. Two criteria need to be met for Rayleigh scattering: (1) The incident field must

be constant across the particle size D ($\pi D/\lambda \ll 1$); and (2) the phase difference between the internal field in the scatterer and applied field should be negligible (i.e., $n2\pi D/\lambda \ll 1$), where n is the refractive index of the scatterer. For most precipitation size particles the second criterion is not satisfied and the approach is not strictly valid for computing phase delay, but the impact of not meeting the second criterion for computing backscatter cross section is minimal. The transition matrix (T-matrix) method is appropriate for computing both backscatter and forward scatter amplitudes of GPS wavelengths from nonspherical scatterers of the size of rain, hail, and snow [*Doviak and Zrnic*, 1993; *Vivekanandan et al.*, 1993].

A precipitation medium contains an ensemble of particles of various sizes, shapes, and bulk density. Much of the atmospheric moisture at altitudes with temperatures below 0°C is ice. Supercooled liquid water seldom exists at temperatures colder than −10°C except in very small droplets. Even though a precipitation event may occur at the surface as rain, there may be ice high in the cloud.

3.4.1. Scattering model computation. We used a rigorous T-matrix approach for computing the scattering characteristics of a nonspherical scatterer such as rain, hail, and snow particles [*Barber and Yeh*, 1975]. Using a single scattering approximation, the T-matrices were averaged over a specified size, shape, and orientation distribution of scatterers. The shape of the scatterer was assumed to be an oblate spheroid. The orientation of the scatterer symmetry axis is assumed to be along the vertical.

The T-matrix essentially relates the unknown scattered field expansion coefficients to the known incident field coefficients (or field transmitted by the GPS signal). Scattering characteristics of raindrops, graupel, and hail particles at microwave frequencies were computed using the T-matrix method [*Aydin and Seliga*, 1984; *Vivekanandan et al.*, 1993]. In this method the incident, scattered, and internal electric fields are expanded in terms of vector spherical harmonics functions, which are composed of associated Legendre functions, sinusoidal functions, and Bessel functions [*Morse and Feshbach*, 1953, chapter 5]. The unknown scattered wave was obtained using a surface integral equation method. The extended boundary condition method and analytic continuity were used to formulate the surface integral equations. The method is ideally suited for axisymmetric particles such as spheroids and cones.

The T-matrix for a particular scatterer of given shape, size, and composition was computed only once with its symmetry axis along the vertical axis. Then to obtain averaged scattering properties of an arbitrarily oriented scatterer, the technique proposed by *Wang* [1979] was used. Depending on the orientation of the scatterer, rotation of the incident and scattered wave directions, as well as rotation of the unit vectors describing the polarization states, were performed to compute the orientation-averaged scattered fields [*Vivekanandan et al.*, 1991].

3.4.2. Phase delay based on scattering for a precipitation medium. Coherent wave propagation through a precipitation medium has been discussed by *Oguchi* [1983]. Consider the propagation path to be uniformly filled with scatterers. Then the propagation phase introduced by the precipitation medium can be written as

$$\phi_{h,v} = 10^{-3} 2 \frac{\pi}{k} \int \mathrm{Re}(f_{h,v}(D)) N(D)\, dD \qquad (9)$$

where $\phi_{h,v}$ is the propagation phase in rad km^{-1}, $k = 2\pi/\lambda$, λ is the GPS wavelength in millimeters, $N(D)$ is the number concentration per cubic meter per size interval in millimeters, D is the equivolumic drop diameter in millimeters, and Re ($f_{h,v}(D)$) is the real part of the forward scattering amplitude in millimeters for horizontal or vertical polarization, as indicated by the subscripts h and v. The scattering amplitude is proportional to frequency and droplet volume:

$$f_{h,v} \propto kV \frac{\varepsilon_r - 1}{\varepsilon_r + 2} \qquad (10)$$

where V is the droplet volume and ε_r is the relative permittivity.

An exponential size distribution of the form

$$N(D) = N_0 e^{-\Lambda D} \qquad (11)$$

was used for rain, ice, and snow precipitation, in units of mm^{-1} m^{-3}. This form of the particle size distribution was chosen for reasons of simplicity, because the moments can be expressed in a closed form. The slope Λ of the size distribution can be calculated from

$$M = \frac{\pi \rho N_0}{1000 \Lambda^4} \qquad (12)$$

where M is the mass content in g m^{-3}, ρ is the assumed bulk density in g cm^{-3}, N_0 is in units of mm^{-1} m^{-3}, and Λ is in units of mm^{-1}.

For raindrops, $N_0 = 8000$ mm^{-1} m^{-3}, and the above described exponential function is called the Marshall-Palmer raindrop size distribution [*Marshall and Palmer*, 1948]. Then the slope Λ is related to rainfall rate R in mm h^{-1} as

$$\Lambda = \frac{4.1}{R^{0.21}} \qquad (13)$$

Raindrops larger than 1 mm in diameter are assumed to be oblate spheroidal in shape due to a balance between surface tension and aerodynamic forces. *Pruppacher and Beard* [1970] show that the ratio of the horizontal to vertical axis r and the equivolumic drop diameter D, in millimeters, are related approximately by

$$r = 1.03 - 0.062\, D \qquad (14)$$

The T-matrix method was used for computing the scattering properties of raindrop sizes between 0.1 and 6.0 mm. Using (9), the propagation phase delay through the rain medium was computed, and results are shown in Figure 1. Rain rates less than 20 mm h^{-1} are considered light rain, 20–60 mm h^{-1} is considered moderate rain, and more than 60 mm h^{-1} is considered heavy rain. Steady rain in Table 2 corresponds to about 20 mm h^{-1}, and the heavy rain value corresponds to about 200 mm h^{-1}.

Propagation delay for hail is shown in Figure 2, assuming a particle bulk density of 0.9 g cm^{-3}, oblate spheroid shape, and an axis ratio of 0.8. Maximum hail size is truncated at 10 mm. Ice water content of the medium varies between 0.01 and 7 g m^{-3}. Propagation delay in hail is 50% of the delay in a comparable rain medium. The delay is lower for ice medium because the permittivity of ice particles is much smaller than the permittivity of raindrops.

The propagation delay for a snow shower is shown in Figure 3. A snow particle is modeled as low-density oblate spheroid. We assumed a bulk density of snowflakes of 0.1 g cm^{-3} and an axis ratio of 0.8. The snow mass content varies between 0.01 and 0.7 g m^{-3}. For a snow shower with 0.7 g m^{-3}, the propagation delay is 0.6 mm for L_2. The lower bulk density reduces delay.

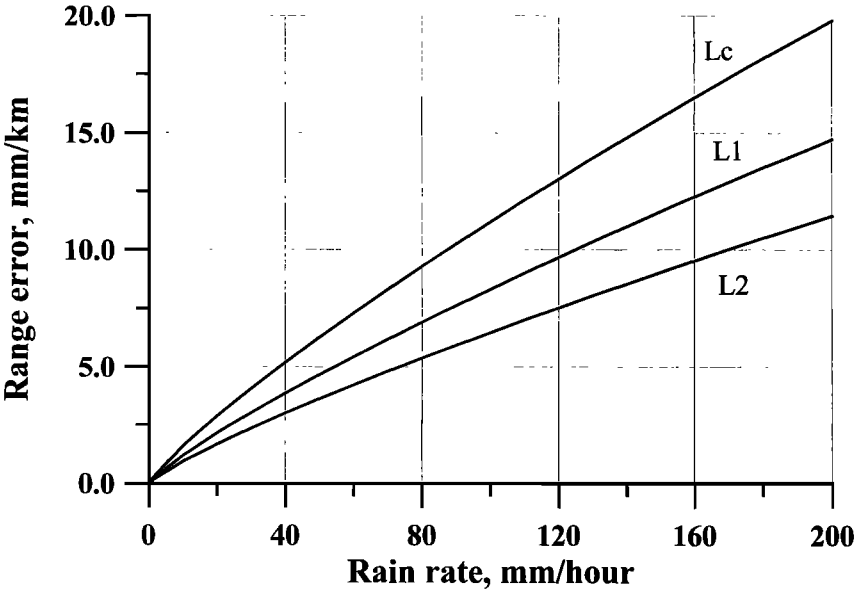

Figure 1. Global Positioning System (GPS) delays for L_1 and L_2 signals due to forward scattering in rain and the resultant range error in L_c.

Figures 1–3 show that the precipitation delays due to scattering are dispersive. Although the GPS signal is transmitted with circular polarization, we present only the delay of a horizontally polarized component. The horizontal and vertical delays can differ depending upon the orientation of the hydrometeors, the elevation angle of the propagation path, and the polarization sensitivity of the GPS receiving antenna.

The L_1 GPS carrier is affected more strongly than the L_2 carrier. Very strong rain rates of 150 mm h^{-1} cause L_1 delays of 12 mm km^{-1} and L_2 delays of 8 mm km^{-1}. In high-precision applications of the GPS we do not directly process L_1 and L_2 data but typically form a linear combination of the L_1 and L_2 GPS phase measurements to cancel the dispersive ionospheric propagation effect on the signal. The ionospheric-free signal (the signal that we would measure if there were no ionosphere between the GPS receiver and transmitter) can be computed from the following linear combination [*Spilker*, 1978]:

$$L_c = \frac{f_1^2}{f_1^2 - f_2^2} L_1 - \frac{f_2^2}{f_1^2 - f_2^2} L_2 \tag{15}$$

This equation is derived from the known dispersive behavior of the ionospheric electron plasma. L_c is the ionospheric free-phase measurement, and L_1 and L_2 are the carrier phase measurements at the f_1 and f_2 nominal GPS carrier frequencies. The equation can be approximated by $L_c = 2.5L_1 - 1.5L_2$. L_1 and L_2 signals that travel through 3 km of 150 mm h^{-1} rain will have phase delays of about 35 and 27 mm, respectively. In the absence of correction for these scattering delays the ionospheric-free linear combination performed in GPS processing will amplify these phase range errors to 47 mm. Corresponding L_3 range errors are shown in Figures 1–3. Even for less extreme rain rates of 50 mm h^{-1} (5 and 4 mm km^{-1} propagation delay according to Figure 1), the effect of propagation through 3 km of rain is almost 20 mm after the standard ionospheric correction

Table 2. Maximum Path Delays Induced by Atmospheric Constituents

Source	Diameter, ≤mm	Surface Density, ≤g m^{-3}	Surface Delay, ≤ mm km^{-1}	Scale Height of Constituent, km	Percentage of Limb Path	Limb Delay, ≤ m
Dry air	10^{-7}	1400	290	8	100	890
High vapor	10^{-7}	25	140	2.7	100	3066
Low vapor	10^{-7}	2.7	15	2.7	100	172
Cloud	0.1	5	8	5	100	107
Radiation fog	0.05	0.1	0.2	0.5	50	11
Advection fog	0.05	0.3	0.3	1	50	11
Haze	0.001	0.01	0.02	2	50	0.5
Drizzle	0.5	0.1	0.2	1.5	50	5.9
Steady rain	4	1	2	3	50	38
Heavy rain	6	7.5	15 (L_2)	6	25	92
Hail	20	7	7 (L_2)	6	5	8.5
Snow	15	.75	0.75 (L_2)	3	50	4.4
Aerosols	0.01	0.1	0.1	0.5	50	5.7
Sand	1	60	18	1	50	205
Volcanic ash	0.2	0.03	0.01	4	50	0.15

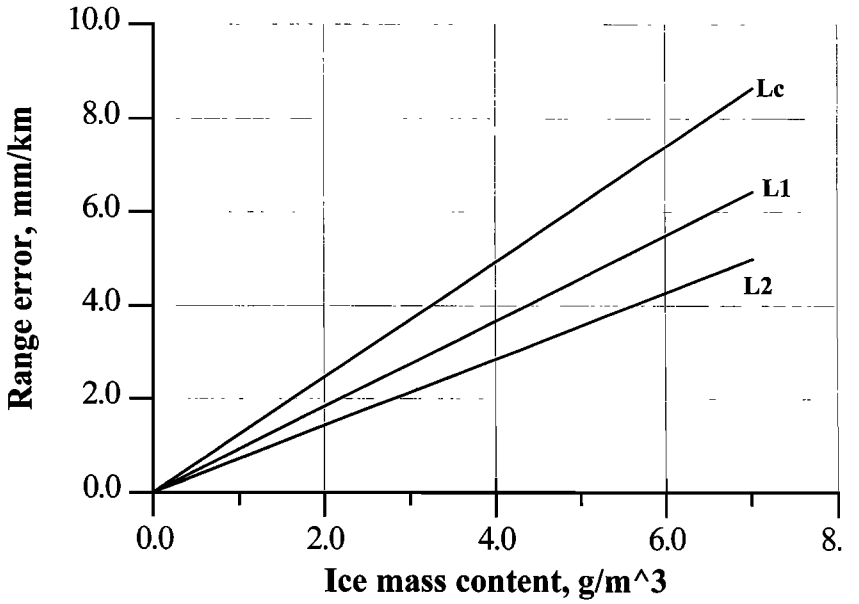

Figure 2. GPS delays for L_1 and L_2 signals due to forward scattering in hail and the resultant range error in L_c.

has been applied. Thus several-centimeter phase delays due to rain may affect low-elevation GPS observations. These errors should be clearly visible in the GPS geodesy data and in GPS estimations of water vapor as compared with radiosondes or radiometers.

4. Limb Delays

Recently, the GPS limb sounding technique has successfully been applied for accurate profiling of the global atmosphere [*Rocken et al.*, 1997b]. Assuming a low Earth orbit (LEO) height of 735 km and a GPS satellite height of 21,000 km, we computed the delay induced by various atmospheric constituents for the limb sounding geometry shown in Figure 4.

The limb delay was computed for different atmospheric refractivity profiles based on the surface refractivity and scale heights listed in Table 2. Profiles were computed assuming exponential decay of surface refractivity with height. For multiple atmospheric constituents with different surface refractivities and scale heights, refractivity from the different constituents at each height level was added. Note that refractivities are additive, but limb delays cannot be added linearly. Because of the amplifying effect of bending angle $\alpha(a)$ upon the phase distance from LEO to GPS satellite, the limb delay induced by a mix of dry air and water vapor is not equal to the limb delay induced by dry air only plus the limb delay for water vapor only. To determine the limb delay, we first calculate the refractivity profile $n(a)$ and then the bending angle according to [*Fjeldbo et al.*, 1971]

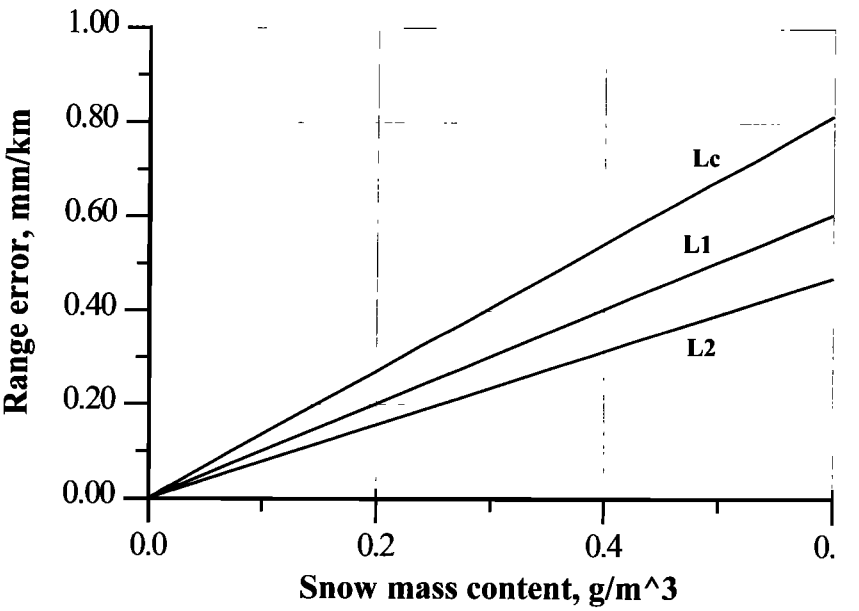

Figure 3. GPS delays for L_1 and L_2 signals due to forward scattering in snow and the resultant range error in L_c.

$$\alpha(a_0) = 2a_0 \int_{a_0}^{\infty} \frac{d \ln n(a)}{da} \frac{1}{\sqrt{a^2 - a_0^2}} da \qquad (16)$$

This integral was solved to determine the bending at a tangent point at the Earth's surface, where r equals the radius of the Earth R_E or $a = R_E n(R_E)$. Once a is known, we compute the delay along the path from the GPS transmitter to the LEO receiver by integration. Finally, the limb delay is defined as this integrated delay minus the straight-line geometric distance from the GPS satellite to the LEO satellite.

Thus the limb delay is the sum of the geometric effect plus the refractive delay along the curved path. The geometric delay depends on the amount of bending, which in turn is a function of vertical refractivity gradients in the atmosphere. Atmospheric constituents with large vertical gradients or small scale heights therefore have large limb delays, primarily due to the geometric effect. The effect of "high water vapor" and "sand" show this effect most dramatically.

Using the above described limb delay calculation, we estimated limb delays for values of surface refractivity and scale height shown in Table 2. Because of the highly variable occurrence and complex distribution of most of the delay-inducing constituents, highly simplified models were employed to approximate real-world limb delays. Exponential lapse rates were assumed in all cases. Each of the atmospheric constituents was added to the base atmosphere of dry air and water vapor, and the additional limb delay was calculated. For heavy rain and hail we assumed that they would occur at most along 25% and 5%, respectively, of the characteristic GPS limb path sampling length of 300 km. This assumption was approximated by applying 25% (or 5%) of the surface refractivity (and the corresponding exponential decay with height) of heavy rain (or hail) to the entire limb path. The "low" vapor value of 2.7 g m^{-3} was utilized to compute the base atmosphere before adding snow (winter) and sand (desert) effects. For all other cases the base atmosphere included the effect of dry air and the high water vapor content (25 g m^{-3}). Clouds were also part of the "base" atmosphere for the drizzle, steady rain, heavy rain, and hail computations.

GPS limb soundings contain a positive refractivity bias, compared with model refractivity, when hydrometeors and particulates are present. This occurs because hydrometeors and particulates are generally not reliably included in meteorological models. The result is apparent high moisture or low temperature values, or a combination, for the GPS limb soundings.

The "limb delay" column in Table 2 shows the additional delay generated by adding the constituent to the base atmosphere. High vapor, for example, adds over 3000 m to the delay incurred by a dry atmosphere, while low vapor adds 172 m.

Maximum path delays induced by dry air and atmospheric constituents in dry air are summarized in Table 2. We list path delays in mm km^{-1} in recognition of the spatial variability of meteorological events. Path delays can be multiplied by the length of the propagation path through the particular medium. For example, a propagation path through a 1-km layer at 15° elevation angle could have delays as large as 500 mm induced by water vapor, 30 mm induced by cloud liquid, 60 mm induced by heavy rain, 30 mm induced by hail, and 3 mm induced by snow. Additionally, dispersive delays due to scattering can alias as ionospheric delay in GPS and very long baseline interferometry data reduction, causing errors.

If the constituencies are uniform across the sky, the resultant delays are absorbed into the zenith delay estimation. However, hydrometeors tend to occur in highly nonuniform distributions. It is because of the broad range of spatial distribution of these constituencies that we do not present modeled results of geodesy positioning errors. Further, we know of no measurement system that can sufficiently define the spatial distribution of hydrometeors and can therefore offer no experimental data.

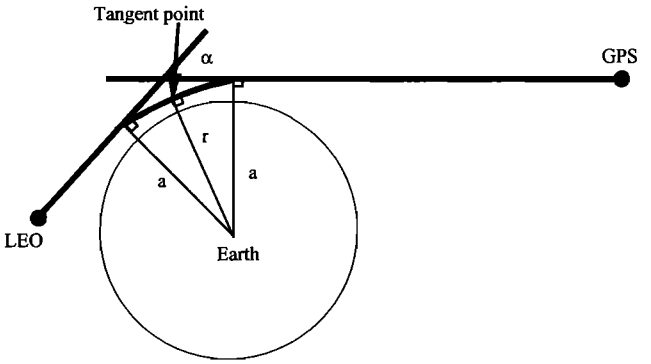

Figure 4. Occultation geometry defining the impact parameter a, the bending angle α, and the radius of the tangent point r.

5. Summary and Conclusions

In summary, atmospheric delays induced by dry air are relatively large and depend on slowly varying pressure fields that are relatively easy to model. Delays induced by water vapor can be as large as 50% of the dry delay (in mm km^{-1}) and are highly variable and not easily modeled. Limb delays induced by water vapor can be more than 3 times as large as those induced by dry air, because of geometric effects. Delays induced by hydrometeors and other particulates are widely variable and are less than 3% of the largest delays induced by dry air and water vapor. Because these highly variable constituents are difficult to quantify, range errors from these constituents cannot effectively be modeled. Proportionate to their magnitude, atmospheric delays present problems in high-accuracy GPS measurement and opportunities for atmospheric remote sensing using GPS.

Acknowledgments. This work was funded by National Science Foundation grants EAR-911756 and EAR-9406153.

References

Adams, R. J., W. F. Perger, W. I. Rose, and A. Kostinski, Measurements of the complex dielectric constant of volcanic ash from 4 to 19 GHz, *J. Geophys. Res.*, *101*, 8175–8185, 1996.

Alber, C., Millimeter precision GPS surveying and GPS sensing of slant path water vapor, Ph.D. thesis, Univ. of Colo., Boulder, Dec. 1996.

Alber, C., R. Ware, F. Solheim, and C. Rocken, GPS surveying with 1-mm precision using corrections for slant path delay, *Geophys. Res. Lett.*, *24*, 1859–1862, 1997.

Aydin, K., and T. A. Seliga, Radar polarimetric backscattering properties of conical graupel, *J. Atmos. Sci.*, *41*, 1887–1892, 1984.

Barber, P., and C. Yeh, Scattering of electromagnetic waves by arbitrarily shaped dielectric bodies, *Appl. Opt.*, *14*, 2864–2872, 1975.

Bar-Sever, Y., P. Kroger, and J. Borjesson, Estimating horizontal gradients of tropospheric path delay with a single GPS receiver, *J. Geophys. Res.*, *103*, 5019–5035, 1998.

Becker, G., and S. Autler, Water vapor absorption of electromagnetic radiation in the centimeter wave-length range, *Phys. Rev.*, *70*, 300–307, 1946.

Bevis, M., S. Businger, T. A. Herring, C. Rocken, R. A. Anthes, and R. H. Ware, GPS meteorology: Remote sensing of atmospheric water vapor using the Global Positioning System, *J. Geophys. Res.*, *97*, 15,787–15,801, 1992.

Born, M., and E. Wolf, *Electromagnetic Theory of Propagation Interference and Diffraction of Light*, 6th ed., chap. 2, pp. 71–108, *Permagon*, Tarrytown, N. Y., 1986.

Brunner, F., and M. Gu, An improved model for the dual frequency ionospheric correction of GPS observations, *Manuscr. Geod.*, *16*, 205–214, 1991.

Businger, S., S. Chiswell, M. Bevis, J. Duan, R. Anthes, C. Rocken, R. Ware, T. Van Hove, and F. Solheim, The promise of GPS in atmospheric monitoring, *Bull. Am. Meteorol. Soc.*, *77*, 5–18, 1996.

Davis, J., G. Elgered, A. Niell, and C. Kuehn, Ground-based measurement of gradients in the "wet" radio refractivity of air, *Radio Sci.*, *28*, 1003–1018, 1993.

Debye, P., *Polar Molecules*, Dover, Mineola, N. Y., 1929.

Dixon, T., An introduction to the Global Positioning System and some geological applications, *Rev. Geophys.*, *29*, 249–276, 1991.

Doviak, R. J., and D. Zrnic, *Doppler Radar and Weather Observations*, 563 pp., Academic, San Diego, Calif., 1993.

Fjeldbo, G., A. J. Kliore, and V. R. Eshleman, The neutral atmosphere of Venus as studied with the Mariner V radio occultation experiments, *Astron. J.*, *76*, 123–140, 1971.

Goldhirsch, J., A parameter review and assessment of attenuation and backscatter properties associated with dust storms over desert regions in the frequency range of 1 to 10 GHz, *IEEE Trans. Antennas Propag.*, *AP-30*, 1121–1127, 1982.

Gross, E., Shape of collision-broadened lines, *Phys. Rev.*, *97*, 395–403, 1955.

Herring, T., The Global Positioning System, *Sci. Am.*, 44–50, Feb. 1996.

Hogg, D., F. Guiraud, and M. Decker, Measurement of excess radio transmission length on Earth-space paths, *Astron. Astrophys.*, *95*, 304–307, 1981.

Hogg, D., F. Guiraud, J. Snider, M. Decker, and E. Westwater, A steerable dual-channel microwave radiometer for measurement of water vapor and liquid in the atmosphere, *J. Clim. Appl. Meteorol.*, *22*, 789–806, 1983.

Jackson, J. D., *Classical Electrodynamics*, 2nd ed., chap. 4, pp. 136–167, John Wiley, New York, 1975.

Keihm, S., M. Janssen, and C. Ruf, TOPEX/Poseidon microwave radiometer (TMR), III, Wet tropospheric range algorithm and prelaunch error budget, *IEEE Trans. Geosci. Remote Sens.*, *33*, 147–161, 1995.

Kuo, Y.-H., X. Zou, S. J. Chen, W. Huang, Y.-R. Guo, R. A. Anthes, M. Exner, D. Hunt, C. Rocken, and S. Sokolovskiy, A GPS/MET sounding through an intense upper-level front, *Bull. Am. Meteorol. Soc.*, *79*, 617–626, 1998.

Kursinski, R., et al., Initial results of radio occultation observations of Earth's atmosphere using the Global Positioning System, *Science*, *271*, 1107–1110, 1996.

Liebe, H., MPM—An atmospheric millimeter-wave propagation model, *Int. J. Infrared Millimeter Waves*, *10*, 631–650, 1989.

Liebe, H. J., T. Manabe, and G. A. Hufford, Millimeter-wave attenuation and delay due to fog/cloud conditions, *IEEE Trans. Antennas Propag.*, *37*, 1617–1623, 1989.

Marshall, J., and W. Palmer, The distribution of raindrops with size, *J. Meteorol.*, *5*, 165–166, 1948.

Meertens, C., C. Rocken, J. Braun, B. Stephens, C. Alber, R. Ware, M. Exner, P. Kolesnikoff, and A. Niell, Antenna type, mount, height, mixing, and snow effects in high accuracy GPS observations, in *The Global Positioning System for the Geosciences*, pp. 211–218, Nat'l. Acad. Press, Washington, D. C., 1997.

Melbourne, W., E. Davis, C. Duncan, G. Hajj, K. Hardy, E. Kursinski, T. Meehan, L. Young, and T. Yunck, The application of spaceborne GPS to atmospheric limb sounding and global change monitoring, *JPL Pub. 94-18*, 147 pp., 1994.

Morse, P., and H. Feshbach, *Methods of Theoretical Physics*, 1978 pp., McGraw-Hill, New York, 1953.

Niell, A., Global mapping functions for the atmosphere delay at radio wavelengths, *J. Geophys. Res.*, *101*, 3227–3246, 1996.

Oguchi, T., Electromagnetic wave propagation and scattering in rain and other hydrometeors, *Proc. IEEE*, *71*, 1029–1077, 1983.

Pruppacher, H., and K. Beard, A wind tunnel investigation of the internal circulation and shape of water drops falling at terminal velocity in air, *Q. J. R. Meteorol. Soc.*, *96*, 247–256, 1970.

Rocken, C., R. Ware, T. Van Hove, F. Solheim, C. Alber, and J. Johnson, Sensing atmospheric water vapor with the Global Positioning System, *Geophys. Res. Lett.*, *20*, 2631–2634, 1993.

Rocken, C., T. Van Hove, J. Johnson, F. Solheim, and R. Ware, GPS/STORM–GPS sensing of atmospheric water vapor for meteorology, *J. Atmos. Oceanic Technol.*, *12*, 468–478, 1995.

Rocken, C., T. Van Hove, and R. Ware, Near real-time sensing of atmospheric water vapor, *Geophys. Res. Lett.*, *24*, 3221–3224, 1997a.

Rocken, C., et al., Verification of GPS/MET data in the neutral atmosphere, *J. Geophys. Res.*, *102*, 29,849–29,866, 1997b.

Segall, P., and J. Davis, GPS applications for geodynamics and earthquake studies, *Annu. Rev. Earth Planet. Sci.*, *25*, 301–336, 1997.

Solheim, F., Use of pointed water vapor radiometers to improve GPS surveying accuracy, Ph.D. thesis, Univ. of Colo., Boulder, Dec. 1993.

Solheim, F., C. Alber, R. Ware, and C. Rocken, Antenna, site, and ancillary data requirements for sensing of slant-path water vapor, in *The Global Positioning System for the Geosciences*, pp. 144–147, Natl. Acad. Press, Washington, D. C., 1997.

Solheim, F., J. Godwin, E. Westwater, Y. Han, S. Keihm, K. Marsh, and R. Ware, Radiometric profiling of temperature, water vapor, and liquid water using various inversion methods, *Radio Sci.*, *33*, 393–404, 1998.

Spilker, J., GPS signal structure and performance characteristics, *J. Inst. Navi.*, *25*, 121–146, 1978.

Thayer, G., An improved equation for the radio refractive index of air, *Radio Sci.*, *9*, 803–807, 1974.

Tranquilla, J. M., and H. M. Al-Rizzo, Range errors in Global Positioning System during ice cloud and snowfall periods, *IEEE Trans. Antennas Propag.*, *42*, 157–165, 1994.

Van de Hulst, H. C., *Light Scattering by Small Particles*, John Wiley, New York, 1957.

Van Vleck, J., *The Theory of Electric and Magnetic Susceptibilities*, Oxford Univ. Press, New York, 1932.

Vivekanandan, J., W. M. Adams, and V. N. Bringi, Rigorous approach to polarimetric radar modeling of hydrometeor orientation distributions, *J. Appl. Meteorol.*, *30*, 1053–1063, 1991.

Vivekanandan, J., R. Raghavan, and V. N. Bringi, Polarimetric radar modeling of mixtures of precipitation particles, *IEEE Trans. Geosci. Remote Sens.*, *31*, 1017–1030, 1993.

Wang, D. Y., Light scattering by nonspherical multilayered particles, Ph.D. thesis, 167 pp., Univ. of Utah, Logan, 1979.

Ware, R., GPS sounding of Earth's atmosphere, *GPS World*, *3*, 56–57, Sept. 1992.

Ware, R., C. Rocken, and K. Hurst, A GPS baseline determination including bias fixing and water vapor radiometer corrections, *J. Geophys. Res.*, *91*, 9183–9192, 1986.

Ware, R., C. Rocken, F. Solheim, T. Van Hove, C. Alber, and J. Johnson, Pointed water vapor radiometer corrections for accurate Global Positioning System surveying, *Geophys. Res. Lett.*, *20*, 2635–2638, 1993.

Ware, R., et al., GPS sounding the atmosphere from low Earth orbit: Preliminary results, *Bull. Am. Meteorol. Soc.*, *77*, 5–18, 1996.

Ware, R., C. Alber, C. Rocken, and F. Solheim, Sensing integrated water vapor along GPS ray paths, *Geophys. Res. Lett.*, *24*, 417–420, 1997.

Waters, J., Absorption and emission by atmospheric gases, in *Methods of Experimental Physics*, edited by M. L. Meeks, chapter 2.3, pp. 142–176, Academic, San Diego, Calif., 1976.

Wen, S., and W. Rose, Retrieval of sizes and total masses of particles in volcanic clouds using AVHRR bands 4 and 5, *J. Geophys Res.*, *99*, 5421–5431, 1994.

Yuan, L., R. Anthes, R. Ware, C. Rocken, W. Bonner, M. Bevis, and S. Businger, Sensing climate change using the Global Positioning System, *J. Geophys. Res.*, *98*, 14,925–14,937, 1993.

C. Rocken, COSMIC Program, University Center for Atmospheric Research, P.O. Box 3000, Boulder, CO 80307. (rocken@ucar.edu)

F. S. Solheim and J. Vivekanandan, Research Applications Program, National Center for Atmospheric Research, P.O. Box 3000, Boulder, CO 80307. (solheim@ucar.edu; vivek@ucar.edu)

R. H. Ware, GPS Science and Technology Program, University Center for Atmospheric Research, P.O. Box 3000, Boulder, CO 80307. (ware@ucar.edu)

(Received August 28, 1998; revised January 19, 1999; accepted February 3, 1999.)